Ab initio study of pressure-driven phase transition in $FePS_3$ and $FePSe_3$

Yueshao Zheng,[1] Xing-xing Jiang,[1] Xiong-xiong Xue,[1] Jiayu Dai,[2] and Yexin Feng[1,*]

[1]*Hunan Provincial Key Laboratory of Low-Dimensional Structural Physics & Devices, School of Physics and Electronics, Hunan University, Changsha 410082, People's Republic of China*

[2]*Department of Physics, National University of Defense Technology, Changsha 410082, People's Republic of China*

(Received 28 July 2019; revised manuscript received 23 October 2019; published 4 November 2019)

In spite of recent findings about the pressure-driven insulator-to-metal phase transition, and emerging superconductivity of $FePS_3$ and $FePSe_3$, the knowledge about their atomic structures is still vague. Here, we investigate the pressure-driven structural phase transitions of $FePS_3$ and $FePSe_3$ from 0 to 35 GPa by using *ab initio* calculations. We find that the $FePS_3$-$C2/m$ B-I structure transforms to the $FePS_3$-$C2/m$ B-II phase at about 5 GPa. Then above 17 GPa, the $FePS_3$-$P\bar{3}1m$ B-III phase becomes energetically favored. For $FePSe_3$, with increasing pressure, the $FePSe_3$-$R\bar{3}$ T-I phase transforms to the B-II phase at around 6 GPa and further to the B-III phase at about 15 GPa. Our calculation results are consistent with experimentally observed high-pressure induced cell volume collapse, spin crossovers, and insulator-metal transition in $FePS_3$ and $FePSe_3$, which shed light on understanding the high-pressure physics and phase transitions of $FePS_3$ and $FePSe_3$.

DOI: 10.1103/PhysRevB.100.174102

I. INTRODUCTION

The transition metal phosphorous trichalcogenides MPX_3 (where $M =$ Mn, Fe, Ni, etc., and $X =$ S, Se) are low-dimensional layered compounds at ambient pressure [1–4]. Due to the weak van der Waals (vdW) interlayer interaction, they are expected to be mechanically exfoliatable [3,5,6]. The S and Se atomic layers stack in the $C2/m$ and $R\bar{3}$ space group, respectively [7]. The transition metal atoms form a graphene-type honeycomb lattice and are enclosed by six S or Se atoms to form an octahedron. Historically, materials from the MPX_3 family (especially $FePS_3$ and $NiPS_3$) serve as good candidates for room temperature Li-based batteries [8–10]. Zhang and co-workers recently proposed that monolayer MPX_3, with band gaps larger than 1.0 eV, are promising photocatalysts for visible-light water splitting [11].

Besides its chemical and catalytic performances, the electronic, magnetic, and superconductive properties of both bulk and single-layer MPX_3 materials are getting more and more research interest [12–25]. Bulk MPX_3 exhibits different kinds of magnetically ordered insulating states. Recently, monolayer MPX_3 was recognized to be one kind of two-dimensional (2D) antiferromagnetic (AFM) material and exhibit valley-dependent optical properties [26]. Transition metal elements play important roles in determining their magnetic ground states. Monolayer $MnPS_3$ and $MnPSe_3$ exhibit Néel antiferromagnetism [5], while $NiPS_3$ and $CoPS_3$ show zigzag antiferromagnetism [21,27]. Chittari *et al.* found that the magnetic phases of these compounds can be controlled through external strains or by modifying the electric field [21]. Due to their rich and interesting magnetic properties, the MPX_3 compounds are expected to be potentially used in spintronic [5,28] and ultrathin magnetic device [15,18].

We focus here on bulk $FePX_3$ ($X =$ S and Se), which exhibits zigzag antiferromagnetism at ambient pressure. $FePS_3$ has an Ising-type AFM structure, with a Néel temperature T_N of 123 K [15]. The high-spin ($S = 2$) Fe^{2+} moments of $FePX_3$ are perpendicular to the *ab* planes. Both $FePS_3$ and $FePSe_3$ are Mott insulators with a band gap of about 1.5 and 1.3 eV, respectively [3,11,29–31]. Wang *et al.* reported that pressure simultaneously induces a semiconductor-to-metal phase transition and a transition from high-spin ($S = 2$) to low-spin ($S = 0$) state at about 13 GPa for $FePS_3$ and 8 GPa for $FePSe_3$, respectively [25]. More interestingly, superconductivity emerges in $FePSe_3$ along with this phase transition with a transition temperature (T_C) ~ 2.5 K at 9 GPa and the maximum $T_C \sim 5.5$ K at about 30 GPa. Almost at the same time, Haines *et al.* found that $FePS_3$ undergoes an insulator-to-metal phase transition under applied high pressure. The low-pressure (LP) phase of $FePS_3$ transforms to the high-pressure (HP) phase HP I at approximately 4 GPa and continues to transform to the HP II phase at around 14 GPa [29]. However, despite these intriguing findings, the details about the high-pressure structures and phase transitions of $FePX_3$ ($X =$ S and Se) are highly unknown. Two kinds of high-pressure structures, HP I and HP II, of $FePS_3$ were proposed in order to explain the pressure-dependent x-ray diffraction (XRD) patterns [29]. However, it still lacks theoretical support, especially concerning the relative stabilities of related structures at varying pressure. For $FePSe_3$, the high-pressure structures are even less explored.

In this work, the pressure-driven structural transitions of $FePS_3$ and $FePSe_3$ were studied by using *ab initio* calculations. The $FePX_3$ family has layered structures with the similar intraplane atomic configurations and different stacking modes. We investigate four kinds of structures for both $FePS_3$ and $FePSe_3$ and study the relative stabilities of them from 0 to 35 GPa. Density functional theory (DFT) $+U$ [32,33] calculations show that the $FePS_3$-$C2/m$ B-I phase

*yexinfeng@pku.edu.cn

and the $FePS_3$-$C2/m$ B-II phase are zigzag antiferromagnetic (ZAFM) states, while the $FePS_3$-$P\bar{3}1m$ B-III phase is a nonmagnetic (NM) state. The pressure of phase transition from the B-I phase to the B-II phase is located at approximately 5 GPa. Upon further increase of pressure up to 17 GPa, the B-II phase is transformed to the B-III phase. For $FePSe_3$, the phase at ambient pressure is different from that of $FePS_3$; it is named the $R\bar{3}$ T-I phase. The first phase transition from the $FePSe_3$-$R\bar{3}$ T-I phase to the B-II phase occurs at approximately 6 GPa. Then at about 15 GPa, the B-II phase transforms to the B-III phase. The proposed structural phase transition sequence well rationalizes experimentally observed pressure-induced insulator-to-metal and high-to-low spin transition, which presents a clear picture for the phase diagram of $FePS_3$ and $FePSe_3$ up to 35 GPa.

II. CALCULATION METHODS

The study on the phase transitions, electronic structures, and magnetic properties of $FePS_3$ and $FePSe_3$, as here reported, was carried out with the density functional theory (DFT) method as implemented in the Vienna *ab initio* simulation package (VASP) [34,35]. The exchange correlation energy is described by the generalized gradient approximation (GGA) using the Perdew-Burke-Ernzerhof (PBE) functional [36]. In order to describe correctly van der Waals interactions resulting from dynamical correlations between fluctuating charge distributions, the semiempirical DFT-D2 method of Grimme was used [37,38]. The nonlocal van der Waals density functional optB86b-vdW was also used to compare with DFT-D2 [39]. The simplified (rotationally invariant) local spin density approximation (LSDA)+U approach introduced by Dudarev *et al.* was used to describe the correlation effects on the localized d orbital of Fe atoms, where the Hubbard effective potential U is 2.5 eV [21,33,40]. The influences of choosing different effective U values and functionals on the phase transition process and band gaps were carefully tested, and are summarized in the Supplemental Material (SM) [41]. The Γ-centered Monkhorst-Pack method with a k-point density of about $2\pi \times 0.03\,\text{Å}^{-1}$ and a plane-wave energy cutoff of 500 eV were used. The convergence criteria for the total energy were set to 10^{-6} eV. Atomic positions and lattice constants of all structures were relaxed until the force was less than 0.02 eV/ Å. In order to accurately calculate the magnetic property of the $FePSe_3 - R\bar{3}$ T-I phase, a $2 \times 1 \times 2$ supercell was used. Phonon dispersions were computed based on the finite-displacement approach as embedded in the PHONOPY program [42]. A $2 \times 1 \times 2$ supercell containing 80 atoms was used for the B-I and B-II phases and a $2 \times 2 \times 2$ supercell for the B-III phase of $FePS_3$. For the T-I, B-II, and B-III phases of $FePSe_3$, $2 \times 2 \times 1$, $2 \times 1 \times 2$, and $2 \times 2 \times 2$ supercells were used, respectively.

III. RESULTS AND DISCUSSION

As mentioned above, the atomic structures of $FePS_3$ and $FePSe_3$ at atmospheric pressure are already known. Although their high-pressure structures are still unclear, two kinds of candidate structures of $FePS_3$ (HP I and HP II) were proposed to explain the high-pressure XRD patterns [29], while the high-pressure structures of $FePSe_3$ are unknown. Based on the ambient pressure structure of $FeP\mathit{X}_3$ and two high-pressure phases (HP I and HP II) proposed by Haines *et al.* [29], as well as the similar intralayer structure and interlayer binding nature of the $FeP\mathit{X}_3$ family, we here investigated four kinds of structures for both $FePS_3$ and $FePSe_3$ at different pressures and renamed them as T-I (trilayer-I), B-I (bilayer-I), B-II (bilayer-II), and B-III (bilayer-III) structures, where B-II and B-III correspond to HP I and HP II, as shown in Fig. 1 and, in the SM, Fig. S1 [41]. In Fig. 1(b) Fe^{2+} forms a

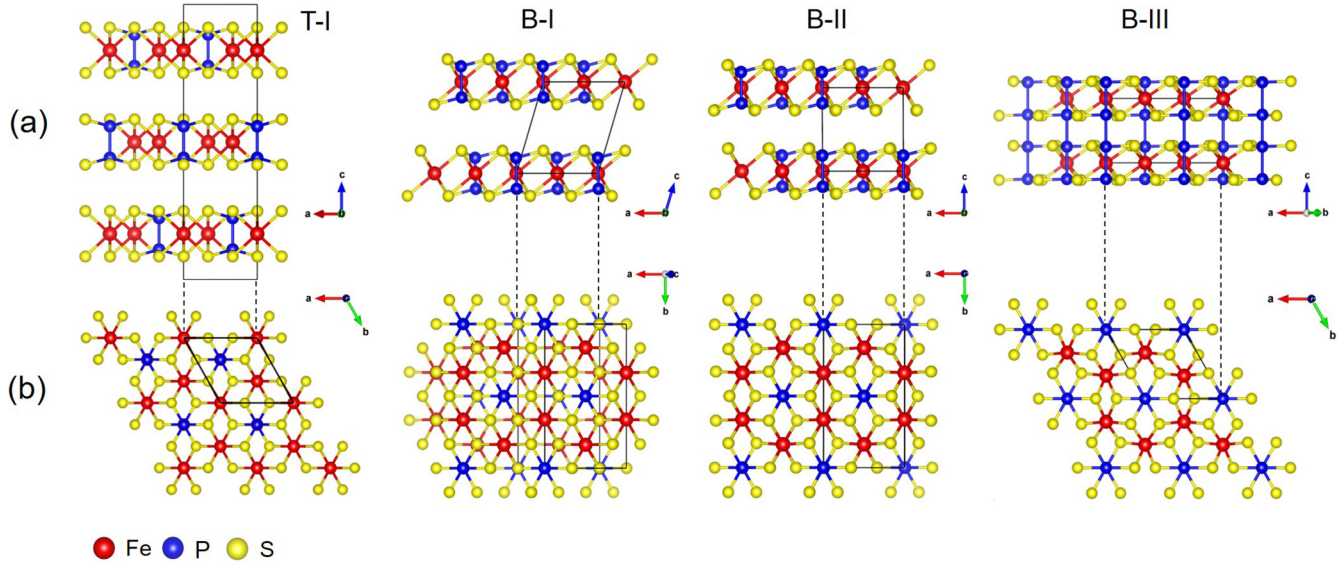

FIG. 1. Crystal structures of $FePS_3$. (a) Side views of T-I, B-I, B-II, and B-III phases. (b) Top views of these phases. Iron atoms form a graphene-type honeycomb lattice and are enclosed by six sulfur atoms to form an octahedron. The example T-I, B-I, B-II, and B-III phases are optimized under 0, 0, 10, and 20 GPa, respectively. The red spheres indicate iron atoms, the blue spheres indicate phosphorus atoms, and the yellow spheres indicate sulfur atoms.

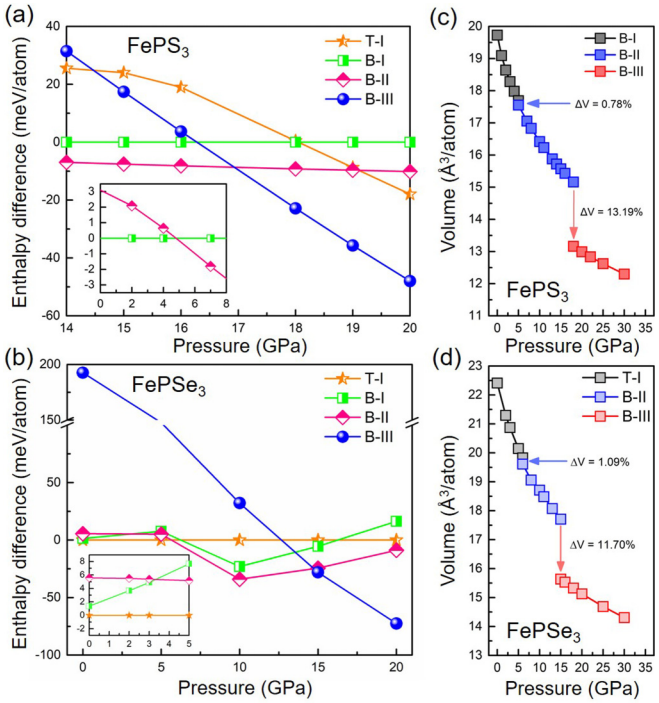

FIG. 2. (a) Enthalpy difference curves (relative to the B-I structures) of the T-I, B-II, and B-III structures as a function of pressure. The inset shows the phase transition from B-I phase to B-II phase at low pressure. (b) Enthalpy difference curves of (relative to the T-I structures) B-I, B-II, and B-III phases of $FePSe_3$. The inset shows enthalpy difference curves at low pressure. (c,d) The derived atom volume values as a function of applied pressure for B-I, B-II, and B-III phases of $FePS_3$ and for T-I, B-II, and B-III phases of $FePSe_3$, respectively.

perfect graphene-type honeycomb lattice, and each Fe atom is enclosed by six S/Se atoms to form an octahedron. P atoms are tetrahedral coordinated with three S/Se atoms. Intralayer P-P pairs are in the center of the octahedron of the S/Se sublattice, forming P_2S_6/P_2Se_6 bipyramid units. At ambient pressure, the T-I and B-I phases of $FeP\mathit{X}_3$ belong to the $R\bar{3}$ and $C2/m$ symmetry groups, respectively, and exhibit ABCABC and inclined AA stacking sequences, respectively. Two high-pressure candidate phases, B-II and B-III, have $C2/m$ and $P\bar{3}1m$ symmetries with the quasipositive AA and positive AA stacking sequences. The B-III structure exhibits a shorter interlayer distance than B-II, even forming interlayer P-P bonds. Due to the high pressure, the B-III phase also shows a staggered arrangement of S/Se atom in each layer.

The enthalpy (H) of all four phases of $FePS_3$ and $FePSe_3$ along with pressure are plotted in Fig. 2. The influence of choosing different functionals and effective U values is shown in Fig. S2 of the SM [41]. With the GGA exchange functional, the first and second phase transition points of $FePS_3$ are observed at about 4.5 and 20 GPa (Fig. S2 [41]), respectively. When considering the interlayer vdW interactions (PBE+D2), the B-I structure transforms to the B-II phase at about 3.3 GPa (Fig. S2(b) [41]), and the B-II phase to the B-III phase at around 17 GPa (Fig. S2(d) [41]).

Although the phase-transition pressures obtained with these two exchange functionals (PBE and PBE+D2) are close to the experimental results [29], the magnetic properties of the B-I and B-II structures fail to be correctively described due to the correlation effects of the localized d orbital of iron atoms. As show in Fig. S3 [41], for the PBE+D2 functional, the B-I phase would transform from the ZAFM to the NM state within its stable pressure range, while for the PBE+D2+U (2.5 eV) functional, the ZAFM state of the B-I phase is always energetically favored within its stable pressure range, which is consistent with the experiment [25]. Using the GGA plus effective U to describe the associated electron-electron correlation effect is an effective scheme. Therefore, we employ the PBE+D2 method with the effective U value of 2.5 eV to study the phase transition evolution and magnetic properties of $FeP\mathit{X}_3$. The results are shown in Fig. 2. The B-I phase of $FePS_3$ is slightly more stable than the B-II phase at 0 GPa with an enthalpy difference less than 3 meV/atom. Above 4.5 GPa, the B-II phase becomes energetically most favored; see inset in Fig. 2(a). As the pressure increases, the $FePS_3$-$C2/m$ B-II phase transforms to the $FePS_3$-$P\bar{3}1m$ B-III phase at about 17 GPa. Within the pressure range of 0–20 GPa, the enthalpy of the T-I phase is always higher than the most stable phases. The above calculation results are close to the phase transitions of about 4 and 13 GPa reported by Haines *et al.* [29]. The dynamic stabilities of relevant structures are also confirmed by phonon calculations. The calculated phonon dispersions for the $FePS_3$-$C2/m$ B-I, $FePS_3$-$C2/m$ B-II, and $FePS_3$-$P\bar{3}1m$ B-III phases are shown in Fig. S6 [41], which confirms that the B-I, B-II, and B-III phases at 0, 10, and 20 GPa are dynamically stable, respectively. The corresponding vibrational energies at 300 K will not affect the phase transition evolution described above. In experiments, the first and second phase transition points of $FePS_3$ occur at approximately 4 and 14 GPa, in good agreement with our simulation results. The detailed discussions about the magnetic properties will be described below.

For $FePSe_3$, as shown in Fig. 2(b), the $FePSe_3$-$R\bar{3}$ T-I phase, instead of the B-I phase, is energetically most stable at 0 GPa, which is also consistent with previous studies. With the increase of pressure, the $FePSe_3$-$R\bar{3}$ T-I phase transforms to the B-II phase and further to the B-III phase at about 5.5 and 15 GPa, respectively. The $FePSe_3$-$C2/m$ B-I phase is always unstable over the pressure range of 0–20 GPa. Again, to verify the dynamic stability of these structures, we calculated phonon dispersion curves for the T-I, B-II, and B-III phases at 0, 10, and 18 GPa, respectively. These three phases are all dynamically stable under the corresponding pressure, as shown in Fig. S7 [41]. It should be noted that, although the low-pressure structures of $FePS_3$ and $FePSe_3$ are different, the high-pressure structure evolutions are similar.

Besides the phase transition pressure, we also investigated the pressure versus cell volume relationships and compare them with experimental observations. The simulation results are shown in Figs. 2(c) and 2(d). Small cell volume decrease (–0.78% at 5.5 GPa and −1.09% at 5 GPa for $FePS_3$ and $FePSe_3$, respectively) can be seen first, which is attributed to structural changes from the B-I phase to the B-II phase for $FePS_3$ and the T-I phase to the B-II phase for $FePSe_3$. The B-II to B-III phase transitions at about 17 GPa ($FePS_3$) and 15 GPa ($FePSe_3$) all lead to a large volume collapses (13.19% and 11.70%), which indicates these phase transitions are first

order with substantial changes of the atomic arrangement. In general, it is significant to have a volume collapse of more than 9% during the phase transition of any other material [43–46], and such large pressure-driven cell volume collapses are thought to be driven by pressure-induced spin crossover [23,25]. The variations in lattice parameters of $FePS_3$ as a function of pressure are also shown in Fig. S8 [41]. The dramatic decreases of c during two phase transitions and of b during the second phase transition indicate that volume collapse occurs on both interlayer and intralayer.

We also investigated the influence of effective U on the phase transition evolutions. The calculated enthalpy-pressure curves of $FePS_3$ with different effective U values are shown in Fig. S4 [41]. As the effective U increases, there is almost no change in the first phase transition point of $FePS_3$, but an obvious change occurs in the second phase transition point. When the effective U value is 3 eV, the second phase transition point is postponed from the original 17 GPa to about 21 GPa, and further to 30 GPa at $U = 4$ eV. We also employed different exchange-correlation functionals with the same value of $U = 2.5$ eV to calculate the enthalpy-pressure relation for $FePS_3$. The results are summarized in Fig. S5 [41].

As mentioned above, correctly dealing with the correlation effects are the key to describing the magnetic properties of $FePX_3$. At ambient pressure, $FePS_3$ is a two-dimensional Ising-type ZAFM phase. Spin moments are ordered ferromagnetically in chains along the a axis, but are in turn antiferromagnetic with adjacent chains, thus reflecting the overall antiferromagnetism. The magnetic structure of the $FePS_3$-$C2/m$ B-I phase is shown in Fig. S9(a) [41]. When the B-I phase transforms to the B-II phase, its magnetic property is still ZAFM (Supplemental Fig. S9(b) [41]). The distribution of the magnetic carriers in $FePSe_3$ is given in Fig. S10 [41]. In order to present a complete magnetic sequence, we build a $2 \times 1 \times 2$ supercell of the $FePSe_3$-$R\bar{3}$ T-I phase. We can find that each Fe^{+2} ion of a single layer is coupled antiferromagnetically with one of the three first neighbors, and then ferromagnetically coupled with the remaining two. When the T-I phase is translated to the B-II phase under high pressure, similar to the case of $FePS_3$, the B-II phase still exhibits interlayer and intralayer ZAFM, as shown in Fig. S10(c) [41]. The high-spin ($S = 2$) Fe^{2+} moments of both phases of $FePS_3$ and $FePSe_3$ are pointing normal to the ab planes from previous studies [1,15,18,24].

The resultant evolution of the Fe^{2+} magnetic moments in $FePS_3$ and $FePSe_3$ with pressure is presented in Fig. 3. At ambient pressure, the $FePS_3$-$C2/m$ B-I and $FePSe_3$-$R\bar{3}$ T-I phases have a high-spin electronic configuration for Fe^{2+} with $S = 2$. As the pressure increases, the magnetic moments decrease slightly until the applied pressure exceeds the B-II to B-III structural transition point of $FePS_3$ (about 17 GPa) and $FePSe_3$ (around 15 GPa), which is slightly higher than ~13 GPa for $FePS_3$ and ~8 GPa for $FePSe_3$ reported in the experiment [25]. More detailed data are shown in Tables S1 and S2 in the Supplemental Material [41]. The magnetic moments decrease to ~0 ($S = 0$) abruptly, indicating that spin crossover leads to a complete collapse of the Fe^{2+} moments in both materials. Like the $MnPX_3$ system [23], the spin crossover in $FePX_3$ is caused by a pure pressure effect. It is well known that the competition between the crystal-field

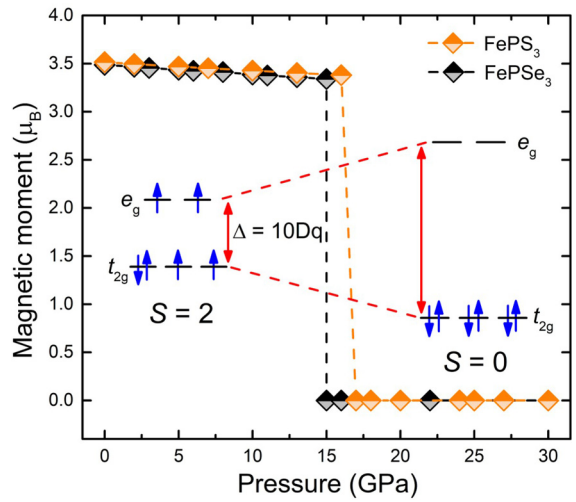

FIG. 3. The magnetic moment values of $FePS_3$ and $FePSe_3$ as a function of pressure. Via pressure-driven spin crossover, $FePS_3$ and $FePSe_3$ go from high-spin ($S = 2$) to low-spin ($S = 0$) states at about 17 and 15 GPa, respectively.

splitting energy $\Delta = 10Dq$ and the Hund's intra-atomic d-d exchange energy J determines the spin state of a transition metal ion [47,48]. As a rule, external pressure hardly affects the parameter J but will increase the splitting energy Δ value. So, when the pressure is high enough, the Δ value will be greater than the parameter J; thus the high-spin state of Fe^{2+} ($S = 2$) will transform to a low-spin state ($S = 0$).

Next, we further calculated electronic band structures of all three phases of $FePS_3$ and $FePSe_3$ using the PBE+D2+U (2.5 eV) method, which gives a more accurate gap. For the first two structures of $FePS_3$ and $FePSe_3$ (zigzag antiferromagnetic phases), the spin-up and spin-down magnetic moments of Fe atoms are equivalent. Therefore, the energy bands with the up and down spins are the same, as shown in Fig. 4. The band gap of the $FePS_3$-$C2/m$ B-I phase is about 1.31 eV, which is an insulator, in agreement with a previous study [3]. From the orbital projected density of states (see Fig. S13 [41]), we can find that electronic states above the Fermi level are mainly derived from the Fe $3d$ and S $3p$ orbitals; below the Fermi level, they are mainly derived from the Fe $3d$ orbitals. For the $FePS_3$-$C2/m$ B-II phase [see Fig. 4(b)], a 1.00-eV band gap at 10 GPa is observed, corresponding to a semiconductor. Like the B-I phase, the bottoms of the conduction bands are largely contributed by the Fe $3d$ and S $3p$ orbitals and the top of the valance bands mainly contain the Fe $3d$ states. In Fig. 4(c), it can be found that the B-III phase is a metal at 20 GPa. Near the Fermi level, it mainly contains the Fe $3d$ and S $3p$ states. We also considered the effect of different effective U values and exchange functionals on the band structures of the B-I and B-II phases, which are shown in Figs. S11 and S12 [41]. Similarly, for the $FePSe_3$-$R\bar{3}$ T-I phase [see Fig. 4(d)], a band gap of 1.24 eV suggests that the T-I phase is an insulator at ambient pressure. When the T-I phase transforms to the B-II phase, the band gap is reduced to 0.72 eV at 10 GPa [Fig. 4(e)]. Then the band structure of the B-III phase shows that it is a metal within its stable pressure range, as shown in Fig. 4(f). The calculated electronic

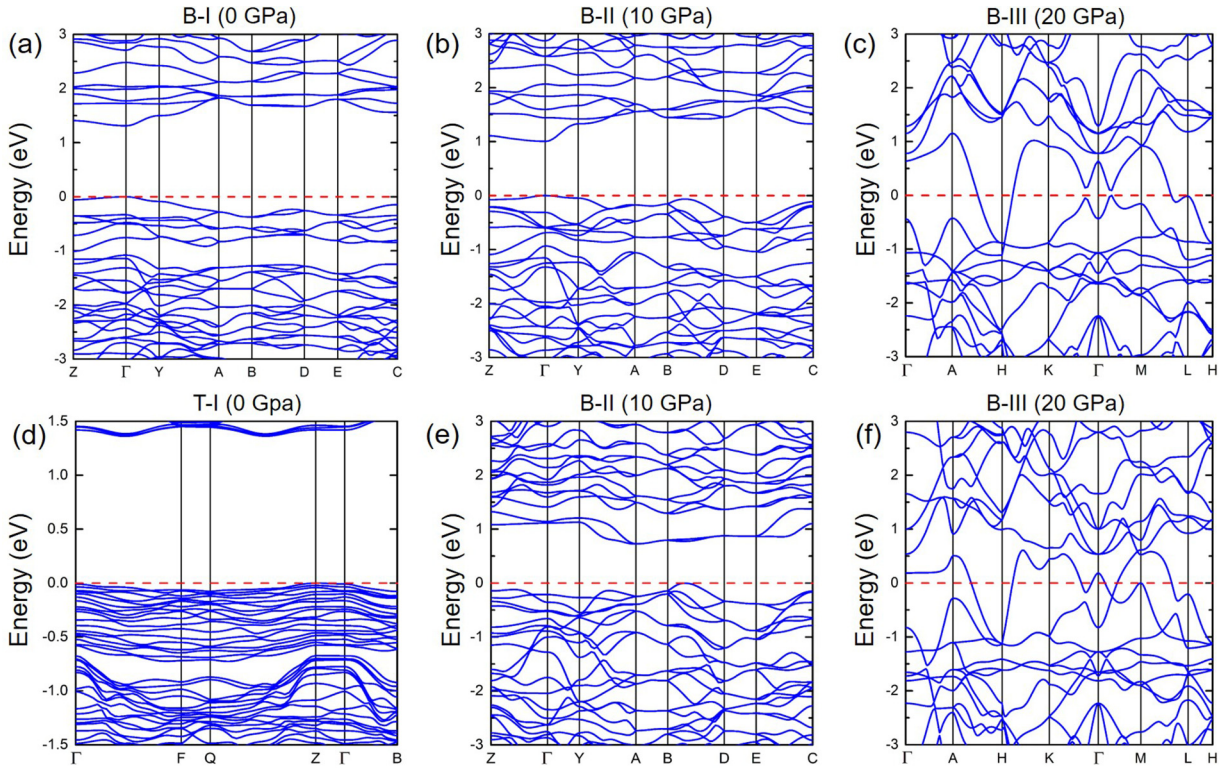

FIG. 4. Band structures along high-symmetry paths for (a) B-I, (b) B-II, and (c) B-III phases of $FePS_3$ and for (d) T-I, (e) B-II, and (f) B-III phases of $FePSe_3$. The top of the valence band is set to be zero in all plots. The band gaps of the B-I and B-II phases of $FePS_3$ are 1.31 and 1.00 eV, and of the T-I and B-II phases of $FePSe_3$ are 1.24 and 0.72 eV. The conduction bands of the B-III phase in both materials overlap with the valence bands. Calculated band structures indicate that $FePS_3$ and $FePSe_3$ translate from insulator to metal under high pressure.

structure evolutions of $FePS_3$ and $FePSe_3$ well rationalize the observed insulator-to-metal transition in experiments.

IV. CONCLUSIONS

In summary, on the basis of *ab initio* (DFT+U) calculations, we studied the pressure-driven phase transitions of $FePS_3$ and $FePSe_3$. We found that for $FePS_3$, the $C2/m$ B-I structure first transforms to the $C2/m$ B-II phase at about 5 GPa, then goes to the $P\bar{3}1m$ B-III phase at about 17 GPa, while for $FePSe_3$, with increasing pressure, the $R\bar{3}$ T-I phase transforms to the B-II phase at around 6 GPa and further to the B-III phase at about 15 GPa. The $FePS_3$-$C2/m$ B-I phase and the $FePS_3$-$C2/m$ B-II phase exhibit interlayer and intralayer zigzag-type antiferromagnetism, and the T-I and B-II phases of $FePSe_3$ show similar magnetic properties. The B-III structure in both materials is the NM state. These results are consistent with experimentally observed pressure-driven spin-crossover behavior. The calculated band structure evolutions also rationalize the insulator-to-metal transition from recent experiments. We believe this study can stimulate more experimental studies about the high-pressure physics and phase transition of $FeP\mathit{X}_3$.

ACKNOWLEDGMENTS

Y.F. and J.D. are supported by the National Basic Research Programs of China with Grant No. 2016YFA0300901; the National Science Foundation of China with Grants No. 11974105, No. 11604092, and No.11774429; and the NSAF under Grant No. U1830206. The computational resources were provided by the supercomputer TianHe in Changsha, China. We also thank Chaoyu He (Xiangtan University) for very useful discussions.

[1] G. Le Flem, R. Brec, G. Ouvard, A. Louisy, and P. Segransan, J. Phys. Chem. Solids **43**, 455 (1982).
[2] A. Wiedenmann, J. Rossat-Mignod, A. Louisy, R. Brec, and J. Rouxel, Solid State Commun. **40**, 1067 (1981).
[3] K. Du, X. Wang, Y. Liu, P. Hu, M. I. B. Utama, C. K. Gan, Q. Xiong, and C. Kloc, ACS Nano **10**, 1738 (2016).
[4] G. Ouvrard, R. Brec, and J. Rouxel, Mater. Res. Bull. **20**, 1181 (1985).
[5] X. Li, X. Wu, and J. Yang, J. Am. Chem. Soc. **136**, 11065 (2014).
[6] C.-T. Kuo, M. Neumann, K. Balamurugan, H. J. Park, S. Kang, H. W. Shiu, J. H. Kang, B. H. Hong, M. Han, T. W. Noh, and J.-G. Park, Sci Rep. **6**, 20904 (2016).
[7] K. Kurosawa, S. Saito, and Y. Yamaguchi, J. Phys. Soc. Jpn. **52**, 3919 (1983).
[8] R. Brec, D. M. Schleich, G. Ouvrard, A. Louisy, and J. Rouxel, Inorg. Chem. **18**, 1814 (1979).
[9] F. S. Khumalo and H. P. Hughes, Phys. Rev. B **23**, 5375 (1981).
[10] N. Kurita and K. Nakao, J. Phys. Soc. Jpn. **58**, 610 (1989).

[11] X. Zhang, X. Zhao, D. Wu, Y. Jing, and Z. Zhou, Adv. Sci. **3**, 1600062 (2016).
[12] S. Bénard, A. Léaustic, E. Rivière, P. Yu, and R. Clément, Chem. Mater. **13**, 3709 (2001).
[13] D. J. Goossens, Eur. Phys. J. B **78**, 305 (2010).
[14] P. A. Joy and S. Vasudevan, Phys. Rev. B **46**, 5425 (1992).
[15] J. U. Lee, S. Lee, J. H. Ryoo, S. Kang, T. Y. Kim, P. Kim, C. H. Park, J. G. Park, and H. Cheong, Nano Lett. **16**, 7433 (2016).
[16] E. Ressouche, M. Loire, V. Simonet, R. Ballou, A. Stunault, and A. Wildes, Phys. Rev. B **82**, 100408(R) (2010).
[17] K. C. Rule, G. J. McIntyre, S. J. Kennedy, and T. J. Hicks, Phys. Rev. B **76**, 134402 (2007).
[18] X. Wang, K. Du, Y. Y. F. Liu, P. Hu, J. Zhang, Q. Zhang, M. H. S. Owen, X. Lu, C. K. Gan, P. Sengupta, C. Kloc, and Q. Xiong, 2D Mater. **3**, 031009 (2016).
[19] A. R. Wildes, V. Simonet, E. Ressouche, G. J. McIntyre, M. Avdeev, E. Suard, S. A. J. Kimber, D. Lançon, G. Pepe, B. Moubaraki, and T. J. Hicks, Phys. Rev. B **92**, 224408 (2015).
[20] V. Zhukov, S. Alvarez, and D. Novikov, J. Phys. Chem. Solids **57**, 647 (1996).
[21] B. L. Chittari, Y. Park, D. Lee, M. Han, A. H. MacDonald, E. Hwang, and J. Jung, Phys. Rev. B **94**, 184428 (2016).
[22] Z. U. Rehman, Z. Muhammad, O. A. Moses, W. Zhu, C. Wu, Q. He, M. Habib, and L. Song, Micromachines **9**, 292 (2018).
[23] Y. Wang, Z. Zhou, T. Wen, Y. Zhou, N. Li, F. Han, Y. Xiao, P. Chow, J. Sun, M. Pravica, A. L. Cornelius, W. Yang, and Y. Zhao, J. Am. Chem. Soc. **138**, 15751 (2016).
[24] D. Lançon, H. C. Walker, E. Ressouche, B. Ouladdiaf, K. C. Rule, G. J. McIntyre, T. J. Hicks, H. M. Rønnow, and A. R. Wildes, Phys. Rev. B **94**, 214407 (2016).
[25] Y. Wang, J. Ying, Z. Zhou, J. Sun, T. Wen, Y. Zhou, N. Li, Q. Zhang, F. Han, Y. Xiao, P. Chow, W. Yang, V. V. Struzhkin, Y. Zhao, and H. K. Mao, Nat. Commun. **9**, 1914 (2018).
[26] X. Li, T. Cao, Q. Niu, J. Shi, and J. Feng, Proc. Natl. Acad. Sci. USA **110**, 3738 (2013).
[27] C. C. Mayorga-Martinez, Z. Sofer, D. Sedmidubsky, S. Huber, A. Y. S. Eng, and M. Pumera, ACS Appl. Mater. Interfaces **9**, 12563 (2017).
[28] A. Brataas and K. M. D. Hals, Nat. Nanotechnol. **9**, 86 (2014).
[29] C. R. S. Haines, M. J. Coak, A. R. Wildes, G. I. Lampronti, C. Liu, P. Nahai-Williamson, H. Hamidov, D. Daisenberger, and S. S. Saxena, Phys. Rev. Lett. **121**, 266801 (2018).
[30] M. Tsurubayashi, K. Kodama, M. Kano, K. Ishigaki, Y. Uwatoko, T. Watanabe, K. Takase, and Y. Takano, AIP Adv. **8**, 101307 (2018).
[31] A. Kamata, K. Noguchi, K. Suzuki, H. Tezuka, T. Kashiwakura, Y. Ohno, and S.-i. Nakai, J. Phys. Soc. Jpn. **66**, 401 (1997).
[32] M. Marsman, J. Paier, A. Stroppa, and G. Kresse, J. Phys.: Condens. Matter **20**, 064201 (2008).
[33] S. L. Dudarev, G. A. Botton, S. Y. Savrasov, C. J. Humphreys, and A. P. Sutton, Phys. Rev. B **57**, 1505 (1998).
[34] G. Kresse and J. Hafner, Phys. Rev. B **48**, 13115 (1993).
[35] G. Kresse and J. Furthmüller, Comput. Mater. Sci. **6**, 15 (1996).
[36] J. P. Perdew, K. Burke, and M. Ernzerhof, Phys. Rev. Lett. **77**, 3865 (1996).
[37] T. Bucko, J. Hafner, S. Lebegue, and J. G. Angyan, J. Phys. Chem. A **114**, 11814 (2010).
[38] S. Grimme, J. Comput. Chem. **27**, 1787 (2006).
[39] J. Klimeš, D. R. Bowler, and A. Michaelides, Phys. Rev. B **83**, 195131 (2011).
[40] A. Hashemi, H.-P. Komsa, M. Puska, and A. V. Krasheninnikov, J. Phys. Chem. C **121**, 27207 (2017).
[41] See Supplemental Material at http://link.aps.org/supplemental/10.1103/PhysRevB.100.174102 for the structures of $FePSe_3$, the phonon dispersions and magnetic structures of $FePS_3$ and $FePSe_3$, the pressure evolution of the lattice parameters through the phase transitions of $FePS_3$, the effect of different functionals with different U values on phase transitions, magnetic properties and band structures, and the orbitally projected density of states (PDOS) of $FePS_3$.
[42] A. Togo, F. Oba, and I. Tanaka, Phys. Rev. B **78**, 134106 (2008).
[43] S. A. J. Kimber, A. Salamat, S. R. Evans, H. O. Jeschke, K. Muthukumar, M. Tomic, F. Salvat-Pujol, R. Valenti, M. V. Kaisheva, I. Zizak, and T. Chatterji, Proc. Natl. Acad. Sci. USA **111**, 5106 (2014).
[44] J. W. Allen and R. M. Martin, Phys. Rev. Lett. **49**, 1106 (1982).
[45] J. Kunes, A. V. Lukoyanov, V. I. Anisimov, R. T. Scalettar, and W. E. Pickett, Nat. Mater. **7**, 198 (2008).
[46] W. Xiao, D. Tan, X. Xiong, J. Liu, and J. Xu, Proc. Natl. Acad. Sci. USA **107**, 14026 (2010).
[47] R. M. Wentzcovitch, J. F. Justo, Z. Wu, C. R. S. da Silva, D. A. Yuen, and D. Kohlstedt, Proc. Natl. Acad. Sci. USA **106**, 8447 (2009).
[48] I. S. Lyubutin, S. G. Ovchinnikov, A. G. Gavriliuk, and V. V. Struzhkin, Phys. Rev. B **79**, 085125 (2009).